The shape-effect of calcium phosphate nanoparticle based films on their osteogenic properties

Biomaterials Science

ROYAL SOCIETY OF CHEMISTRY

PAPER

View Article Online
View Journal | View Issue

Cite this: *Biomater. Sci.*, 2021, **9**, 1754

The shape-effect of calcium phosphate nanoparticle based films on their osteogenic properties†

Pichaporn Sutthavas, Pamela Habibovic and Sabine H. van Rijt *

Calcium phosphates (CaPs) in the form of hydroxyapatite (HA) have been extensively studied in the context of bone regeneration due to their chemical similarity to natural bone mineral. While HA is known to promote osteogenic differentiation, the structural properties of the ceramic have been shown to affect the extent of this effect; several studies have suggested that nanostructured HA can improve the bioactivity. However, the role shape plays in the osteogenic potential is more elusive. Here we studied the effect of HA nanoparticle shape on the ability to induce osteogenesis in human mesenchymal stromal cells (hMSCs) by developing nanoparticle films using needle-, rice- and spherical-shaped HA. We showed that the HA films made from all three shapes of nanoparticles induced increased levels of osteogenic markers (*i.e.* runt-related transcription factor 2 (RUNX2), bone morphogenetic protein 2 (BMP2), alkaline phosphatase (ALP), osteopontin (OPN), osteocalcin (OCN) on protein and gene level in comparison to hMSCs cultured on cover glass slides. Furthermore, their expression levels and profiles differed significantly as a function of nanoparticle shape. We also showed that nanoparticle films were more efficient in inducing osteogenic gene expression in hMSCs compared to adding nanoparticles to hMSCs in culture media. Finally, we demonstrated that hMSC morphology upon adhesion to the HA nanoparticle films is dependent on nanoparticle shape, with hMSCs exhibiting a more spread morphology on needle-shaped nanoparticle films compared to hMSCs seeded on rice- and spherical-shaped nanoparticle films. Our data suggests that HA nanoparticle films are efficient in inducing hMSC osteogenesis in basic cell culture conditions and that nanoparticle shape plays a vital role in cell adhesion and morphology and extent of induction of osteogenic differentiation.

Received 4th September 2020,
Accepted 6th January 2021

DOI: 10.1039/d0bm01494j

rsc.li/biomaterials-science

1. Introduction

Calcium phosphate (CaP) ceramics are extensively used materials in the field of bone regeneration due to their inherent ability to stimulate and facilitate bone formation *in vivo*.[1–6] CaP ceramics are chemically similar to the inorganic component of human bone, which is composed of nano-sized CaP crystals in the form of hydroxyapatite (HA). To circumvent the drawbacks associated with autologous bone grafts, which include limited availability and donor site complications, researchers have focused on developing synthetic HA-based bone graft substitutes. Synthetic HA ceramics have demonstrated excellent biocompatibility and bioactivity in terms of osteoconductivity and bone-bonding potential.[7–15] Amongst other applications, HA ceramics have gained interest for use as coatings on (metallic) implants to improve cell adhesion and increase bone-to-implant contact *in vivo*.[16–19] While HA is generally accepted as a bioactive material in a bony environment, the chemical and structural characteristics of the HA surface highly affect the extent and the type of interactions between the material and the local (cellular) environment. For example, the chemical composition influences cellular interactions with the surface and can be employed to tune protein adsorption on a material, a pre-requisite for cell attachment.[20,21] Additionally, the ceramic itself can affect the dynamics of calcium and phosphate ions exchange with the microenvironment, which in turn may favour the deposition of new bone matrix.[22–24] The HA surface structure, the so-called surface topography, can also modulate cellular behaviour where it has been shown that especially structural features at the nanoscale can positively influence cell adhesion and subsequent hMSC proliferation and differentiation.[25–28]

A popular way to create nanostructured HA coatings is by depositing nano-sized HA particles on implant surfaces.[29–31]

Department of Instructive Biomaterials Engineering, MERLN Institute for Technology-Inspired Regenerative Medicine, Maastricht University, P.O. Box 616, 6200 MD Maastricht, The Netherlands. E-mail: s.vanrijt@maastrichtuniversity.nl

†Electronic supplementary information (ESI) available. See DOI: 10.1039/d0bm01494j

Driven by the popularity and potential of HA nanoparticles (nHA) in the field of bone regeneration but also in the field of drug delivery,[32,33] many methods have been reported to chemically synthesize nHA including various wet and dry synthesis methods.[30,33–37] However, obtaining nHA with homogeneous shape and size remains challenging. This is especially true for wet chemical precipitation methods as calcium and phosphate ions can spontaneously precipitate and crystallize above pH 7. As a result, the effect of nHA shape on the ability to induce osteogenic differentiation in hMSCs is much less studied, although several studies hint that nHA shape plays an important role in their osteogenic effect. For example, Xu *et al.*[38] showed that osteoblasts cultured with needle-shaped nHA increased cell proliferation and upregulated alkaline phosphatase (ALP) and osteocalcin (OCN) expression after 4 days, compared to osteoblasts exposed to spherical nHA. Another study reported that HA nanospheres triggered a stronger osteogenic effect in hMSCs compared to HA nanorods.[39] In contrast, Liu *et al.* reported a relatively limited effect of spherical nHA on its ability to promote osteogenic differentiation in hMSCs under standard culture conditions.[40] Importantly, these studies were performed under conditions where HA nanoparticles were directly added to the cell culture media of hMSCs adhered to the surface, and their osteogenic effect was related to hMSC cellular uptake of nHA. The effect of different nanoparticle shapes on their osteogenic potential when deposited in the form of stable coatings has, to our knowledge, not yet been studied.

Here we synthesized needle-, rice- and spherical-shaped nHA and used these to deposit homogeneous films on glass slides. We investigated the effect of nanoparticle shape on the expression profiles of different stage osteogenic markers in primary hMSCs. Specifically, we investigated the effect of nanoparticle shape on bone morphogenetic protein 2 (BMP2), and runt-related transcription factor 2 (RUNX2) which are important markers in the first stage of bone formation where mesenchymal precursors commit to osteoblast differentiation lineage. In addition, we investigated the effect of nHA shape on ALP, osteopontin (OPN), and OCN, which are good indicators of middle to later stage bone formation where there is an increase of metabolic activity and bone cells deposit and mineralize matrix.[41] In addition, the morphology and adhesion of hMSCs on the different nanoparticle films were analysed. Finally, the ability of nanoparticles to induce osteogenic differentiation when added as single particles to the cell culture medium and nanoparticle conditioned media was compared to osteogenic marker expression of hMSCs cultured on the nHA films.

2. Experimental

2.1. Materials

Tetraethyl orthosilicate (TEOS), 3-mercaptopropyl triethylsilane (MPTES), triethanolamine (TEA), 3-aminopropyl triethoxysilane (APTES), cetyltrimethylammonium chloride (CTAC), cetyltrimethylammonium bromide (CTAB), ammonium fluoride, hydrochloric acid (37%), ammonium nitrate, *N*,*N*-dimethylformamide (DMF), phosphate-buffered saline (PBS), foetal bovine serum, ascorbic acid, bis[*N*,*N*-bis(carboxymethyl) aminomethyl] were purchased from Sigma Aldrich GmbH (Germany). Absolute ethanol, paraformaldehyde (PFA), Triton X-100, bovine serum albumin (BSA), Tween-20 and Alizarin Red S (sodium alizarin sulphonate) were purchased from VWR (US). Minimum essential medium alpha (αMEM), L-glutamine and trypsin were purchased from Fisher Scientific (The Netherlands). Penicillin and streptomycin were purchased from Gibco Life Technologies (US).

2.2. Synthesis of needle-shaped HA nanoparticles

To produce needle-shaped nanoparticles, 0.6 mM calcium nitrate and 0.4 mM potassium phosphate salt solutions in milliQ water (40 ml) were prepared. Both salt solutions were slowly added dropwise *via* a syringe pump at 2 ml per min into a reactor containing 100 ml milliQ water under rigorous stirring. The reaction was kept at pH 10 by adding ammonium nitrate. After 20 minutes, 1 ml of a 6 μM calcium nitrate solution was added to the mixture. To stop crystal growth, 1 ml 4 μM phosphate-polyethylene glycol (phosphate-PEG) solution was added to the reactor immediately after addition of calcium nitrate solution. Afterwards the mixture was washed three times with absolute ethanol using centrifugation. The slurry was then dried overnight before sintering at 800 °C for 12 hours to remove PEG chain from the surface.

2.3. Synthesis of rice-shaped HA nanoparticles

In order to achieve rice shape HA nanoparticles, CTAB was used as a template. 0.6 mM calcium nitrate and 0.4 mM potassium phosphate solutions were slowly added dropwise *via* a syringe pump at 2 ml per min into 1 mM of CTAB in milliQ water under the rigorous stirring. After washing with absolute ethanol three times, the CTAB template was removed *via* ion exchange reactions under basic conditions: nanoparticles were resuspended in 100 ml absolute ethanol with 100 mg of NH_4NO_3 for 45 minutes at 90 °C under reflux conditions. The rice nanoparticles were then washed again with absolute ethanol before further use.

2.4. Synthesis of spherical nanoparticles

Mesoporous silica nanoparticles (MSNs) were used as hard templates for calcium and phosphate ion deposition. MSNs with amine surface functionalization were synthesized *via* modified co-condensation methods as reported previously.[42] The amine groups on the MSN surface were further modified to obtain carboxylic acid groups, which allowed positive ion deposition. Carboxyl-functionalized MSN nanoparticles (MSN-COOH) were obtained as follows: 3 g of succinic anhydride was added in 20 ml DMF, and allowed to fully dissolve for 30 minutes at room temperature (solution 1). Subsequently, 0.2 g of MSNs were dispersed in 30 ml DMF, and the suspension was added into solution 1 under magnetic stirring. The reaction was kept at 60 °C for 48 h. Afterwards,

the suspension was collected by centrifugation and extensively washed with absolute ethanol. MSN-COOHs were resuspended in milliQ water adjusted to pH 10 by NH_4NO_3. Afterwards, 200 μl 6 μM calcium nitrate solution was added to the mixture and allowed to react for 30 min. The mixture was then washed with milliQ water once before adding 200 μl 4 μM of $(NH_4)_3PO_4$ solution, and subsequently washed with absolute ethanol. The process of calcium ions and phosphate ions addition was repeated two more times.

2.5. Characterization of the nanoparticles

Zeta potential and polydispersity index (pdi) of all nanoparticles were measured on a Malvern Zetasizer Nano (Malvern Panalytical, UK). For the analysis, nanoparticles were suspended in ethanol at a concentration of 0.3 μg ml^{-1}. Morphology of all nanoparticles was further visualized by scanning electron microscopy (SEM; Teneo, FEI, US). For SEM analysis, dry nanoparticle powder was suspended in absolute ethanol, a drop was placed on an aluminium SEM stub and allowed to dry overnight. The samples were sputtered with a 2 nm layer of iridium before imaging. X-ray diffractograms (XRD) of all HA nanoparticles were collected using a Bruker D2 Phaser diffractometer (Bruker) using Cu Kα radiation (λ = 1.542 Å) in the range of $6 \leq 2\Theta \leq 60°$ in increments of 0.02° and an integration time of 0.5 s.

2.6. Thin film formation and characterization

Prior to spinning, cover slips were surface-activated with O_2 plasma treatment (Plasma Cleaner, Diener Electronics Femto PCCE) at 0.4 bar, 5 sscm O_2, 70 W, 1.5 min. All nanoparticles were collected by centrifugation (14 000 rpm, 20 °C, 10 min) and dispersed in absolute ethanol at a concentration of 50 μg ml^{-1}. A volume of 20 μl of the suspension was pipetted centrally on a cover slip and spun at 2000 rpm for 20 s and then at 7000 rpm for 30 s on a tabletop spin coater. The obtained films were stored dry at room temperature in the dark. To characterize the films, three-dimensional laser scanning microscopy (Keyence VR-200 3D Profilometer, Keyence, Japan) was used to estimate film thickness and surface roughness.

2.7. Thin film stability

To investigate the stability of nanoparticles thin films in aqueous environment and cell culture medium, nHA films were immersed in either 2 ml PBS at pH 7.4 or cell culture medium (αMEM with 10% v/v 100× penicillin and streptomycin) and incubated at room temperature. 20 μl of solution were taken for analysis at 1, 3, 6, 24, 72 and 144 hours upon nHA film immersion. The concentration of calcium and phosphorus was quantitatively studied by inductively coupled plasma mass spectroscopy (ICP-MS, iCaP Q, Thermo Scientific). To this end, aliquots were diluted 1 : 200 in aqueous 1% HNO_3 containing 20 ppb Sc as internal standard and analysed using He as collision gas in standard mode. Element quantification was based on calibrations with element standards of calcium and phosphorus.

2.8. *In vitro* cell culture

hMSCs of one donor, obtained with written consent, were expanded in αMEM with addition of 10% FBS, 2 mM L-glutamine, 0.2 mM ascorbic acid, 100 U ml^{-1} penicillin and 100 mg ml^{-1} streptomycin at 37 °C, 5% CO_2 in a humidified atmosphere. Cells of passage 4 were used for experiments. The cells were seeded at a density of cells per cm^2. For cell seeding, 250 μl of cell suspension was carefully pipetted on the all nanoparticle films, or uncoated glass cover slips, and cells were left to adhere for 6–8 h before addition of 2 ml medium.

2.9. Quantitative polymerase chain reaction (qPCR)

The effect of nanoparticle shape on osteogenic differentiation of hMSCs was evaluated by measuring expression of osteogenic markers (RUNX2, BMP2, ALP, OPN, OCN) after 7, 14 and 21 of culture, respectively. hMSCs expanded in basic medium were detached at a confluence of 70–80% and seeded on nanoparticles films. Cells grown on uncoated, O_2 plasma surface-activated cover slips were used as control. hMSC basic medium were refreshed every 3 days.

Total RNA was isolated from hMSCs cultured on thin films *via* the Trizol method. RNA was further purified using RNA isolation kit (Bioline ISOLATE II RNA Mini Kit) and the total concentration was measured using the nanodrop method (Thermo Scientific NanoDrop). The cDNA was then prepared using an iScript kit (Bio-Rad) according to the manufacturer's protocol and kept in RNAse free water to be used for qPCR (Bio-Rad) using Syber Green I master mix (Invitrogen). The primer sequences (Sigma) are listed in Table 1. Expression of osteogenic marker genes were normalized to GAPDH levels and basic fold indications were calculated by using ΔΔCT method. hMSCs cultured on plasma cleaned cover slides in basic medium for 7 days were used as calibrator. Two independent experiments with n = 3 for each condition were performed for the qPCR analysis and the results of one representative experiment are presented here.

2.10. Nanoparticle suspension experiments

The osteogenic effect of the nHA applied as a film, as suspensions in the cell culture medium, and nanoparticle-conditioned medium (containing ions released from nanoparticles) was determined. For this, 3 osteogenic markers; ALP, OPN and OCN were quantified using qPCR analysis after 21 days of culture. Two types of nanoparticles, needle and spherical nHA were chosen for this comparison. hMSCs were detached at a confluence of 70–80% and seeded on nanoparticles films. Cells grown on uncoated, O_2 plasma surface-activated cover slips were used for the other two groups. The same amount of nHA in weight that was used to coat the films was added to the cell culture medium (32 μg ml^{-1} for needle nanoparticles and 43 μg ml^{-1} for spherical nanoparticles) to create suspension medium and divided over the duration of the experiment. To create the conditioned medium, the cell culture medium was incubated with spherical or needle shaped nanoparticles overnight. This was then centrifuged at 3000 rcf and the supernatant was used in the cell culture

Table 1 Primer sequence of the osteogenic genes investigated

Gene	Primer sequences
Glyceraldehyde 3-phosphate dehydrogenase (GAPDH, housekeeping gene)	5′-CCATGGTGTCTGAGCGATGT 5′-CGCTCTCTGCTCCTCCTGTT
Runt-related transcription factor 2 (RUNX 2)	5′-GGAGTGGACGAGGCAAGAGTTT 5′-AGCTTCTGTCTGTGCCTTCTGG
Bone morphogenetic protein 2 (BMP2)	5′-GCATCTGTTCTCGGAAAACCT 5′-ACTACCAGAAACGAGTGGGAA
Alkaline phosphatase (ALP)	5′-TTCAGCTCGTACTGCATGTC 5′-ACAAGCACTCCCACTTCATC
Osteopontin (OPN)	5′-CCAAGTAAGTCCAACGAAAG 5′-GGTGATGTCCTCGTCTGTA
Osteocalcin (OCN)	5′-CGCCTGGGTCTCTTCACTAC 5′-TGAGAGCCCTCACACTCCTC

experiments. For all conditions, the medium was refreshed every 3 days for the duration of the experiment. qPCR analysis was performed as described in 2.9.

2.11. Western blot

Proteins were isolated from cells cultured on films in RIPA buffer (Sigma-Aldrich), supplemented with cOmplete™, Mini, EDTA-free Protease Inhibitor Cocktail (Sigma-Aldrich). To obtain sufficient protein amounts, cells from two films were mixed into 400 µl lysis buffer for a single protein isolation. Experiments were repeated three times for biological triplicates. Film surfaces were scraped with cell scrapers and samples were centrifuged. Protein quantification was done using the Pierce BCA protein assay kit (Thermo Fisher Scientific). Twenty micrograms of protein was incubated with laemmli loading buffer (Bio-Rad) and 10% 2-mercaptoethanol (Sigma-Aldrich) for 5 min at 95 °C and loaded into a 4–15% polyacrylamide gel (Bio-Rad). Proteins were transferred to a 0.45 µm PVDF membrane (Bio-Rad) using the semi-dry transfer method. Membranes were blocked for 1 h with 5% fat free milk powder (Bio-Rad) in TBS + 0.05% tween-20 (Sigma-Aldrich). OPN and GAPDH antibody incubations were performed overnight at 4 °C in blocking buffer. All antibodies were ordered from Abcam and diluted 1/1000, except for RUNX2 which was diluted 1/500. Blots were subsequently incubated with 0.33 µg ml^{-1} goat-anti-rabbit or mouse horseradish peroxidase (Bio-Rad) in blocking buffer for 1 h at room temperature. Protein bands were then visualized using Clarity Western ECL (Bio-Rad).

2.12. Cell morphology analysis

To conserve cells for morphological analysis, hMSCs were fixed using 4% PFA in PBS, 3 days after cell seeding. Samples were stored in PBS at 4 °C until staining. After fixation, hMSCs were permeabilized with 0.2% Triton X-100 in PBS solution for 1 h. Cells were washed with PBS and subsequently stained with phalloidin Alexa Flour 647 antibody (Invitrogen) at room temperature in the dark for 2 h. After incubation, cells were washed with PBS twice and stained with DAPI antibody (Sigma-Aldrich/Fluka) for 15 minutes. The cells were then washed with PBS and imagined using a Nikon Eclipse Ti-E microscope (Nikon Instruments Europe BV, the Netherlands) at 40× magnification. Images were acquired with a Zyla sCMOS (Andor Technology Ltd, UK) and a Nikon DS-Ri2 camera (Nikon Instruments Europe BV, the Netherlands). Cells stained with phalloidin and DAPI were used for quantitative analysis of cell morphology. The data was analysed in CellProfiler software. Cell morphology was quantified in terms of cell area (measured by the number of pixels occupied) and cell perimeter (total number of pixels (2D) around the boundary of each object in the image), eccentricity (morphological elongation expressed as the deviation from a circle with values between 0 and 1, where 0 is a circle and 1 is a line segment), and compactness (mean squared distance of the object pixels from the centroid divided by the area. A filled circle will have a compactness of 1, with irregular objects or objects with holes having a value greater than 1). A schematic of this data analysis process is shown in ESI Fig. S5.†

2.13. Cell adhesion experiments

Cellular adhesion on nanoparticle films was analyzed by immunohistochemical staining of the focal adhesion protein vinculin. hMSCs were seeded on at a density of 3000 cells per cm^2. After 3-day culture, cells were fixed with 4% PFA. Prior to staining, cells were washed once with PBS and permeabilized with Triton X-100 (0.01% (vol/vol) in PBS) for 10 min at room temperature followed by washing three times with PBS. Samples were then incubated for 60 min in blocking buffer (4% BSA and 0.05% (vol/vol) Tween-20 in PBS) at room temperature. Mouse monoclonal IgG1 anti-vinculin antibody (SPM227, 1 : 500; Abcam) was used as the primary antibody and incubated with the cells overnight at 4 °C in the dark. The samples were then washed with washing buffer (blocking buffer diluted 1 : 5 in PBS) and incubated overnight at 4 °C with the secondary antibody, biotin-conjugated, rabbit anti-mouse IgG1 (1 : 1000; Sigma Aldrich). After washing, samples were incubated for 1 h with streptavidin Alexa FluorTM 647 conjugate (1 : 200; Fisher Scientific), followed by washing 3 times with washing buffer. All antibody dilutions were prepared with washing buffer (blocking buffer diluted 1 : 5 in PBS). To visualize actin bundles, cells were stained with Alexa FluorTM 488 phalloidin (1 : 200 in PBS; Thermo Fisher

Scientific) for 30 min at room temperature, followed by washing three times with PBS. To visualize cell nuclei, samples were incubated for 6 min with 4′,6-Diamidin-2-phenylindol (DAPI, 1 : 70 in PBS; Sigma Aldrich) at room temperature, washed three times with PBS and mounted with Dako® (Sigma Aldrich). Cells were imaged with a Nikon Eclipse Ti-E microscope (Nikon Instruments Europe BV, the Netherlands) using an oil objective. Images were further processed and merged using ImageJ.

2.14. Statistical analysis

Statistical comparisons were performed using one-way analysis of variance (ANOVA) followed by a Turkey's multiple comparison *post-hoc* test. Error bars indicate one standard deviation. For all figures the following p-values apply: $*p < 0.01$; $**p < 0.01$; $***p < 0.001$.

3. Results and discussion

3.1. Needle-, rice- and spherical-shaped nHA synthesis and characterization

Three types of nHA (needle-, rice- and spherical-shaped) were successfully synthesized (Fig. 1a). To develop the needle-shaped nHA (Fig. 1a, left panel), calcium and phosphate ions were precipitated while maintaining the pH at 10 using an ammonium solution. To synthesize the rice-shaped nanoparticles, structure-directing agent CTAB was used to form micelles which restricted the crystal growth by surrounding the particles. This closure caused thickening of the particles in comparison to needle-shaped nHA, resulting in formation of rice-shaped nanoparticles (Fig. 1a, middle panel). After nanoparticle synthesis, CTAB was removed using ion exchange in a basic environment. To develop spherical CaP nanoparticles, MSNs were used as a template for calcium and phosphate ion deposition. MSNs with amine surface functionalization were synthesized *via* modified co-condensation methods as reported previously.[42,43] The amine groups on the MSN surface were further modified to obtain carboxylic acid groups to allow positive ion deposition. Calcium and phosphate sources were added alternately to create a CaP layer on the MSN surface (Fig. 1a, right panel).

The hydrodynamic size of the nHA and their pdi in an ethanol solution were measured using dynamic light scattering (DLS). All three nanoparticle types were similar in size, with hydrodynamic sizes of 240 ± 40 nm, 230 ± 20 nm and 250± 10 for needle-, rice- and spherical-shaped nanoparticles, respectively (Fig. 1b). The nanoparticles were monodisperse with pdi indices of 0.31 (needle-shaped), 0.26 (rice-shaped) and 0.30 (sphere-shaped). Thus, all three methods enabled the for-

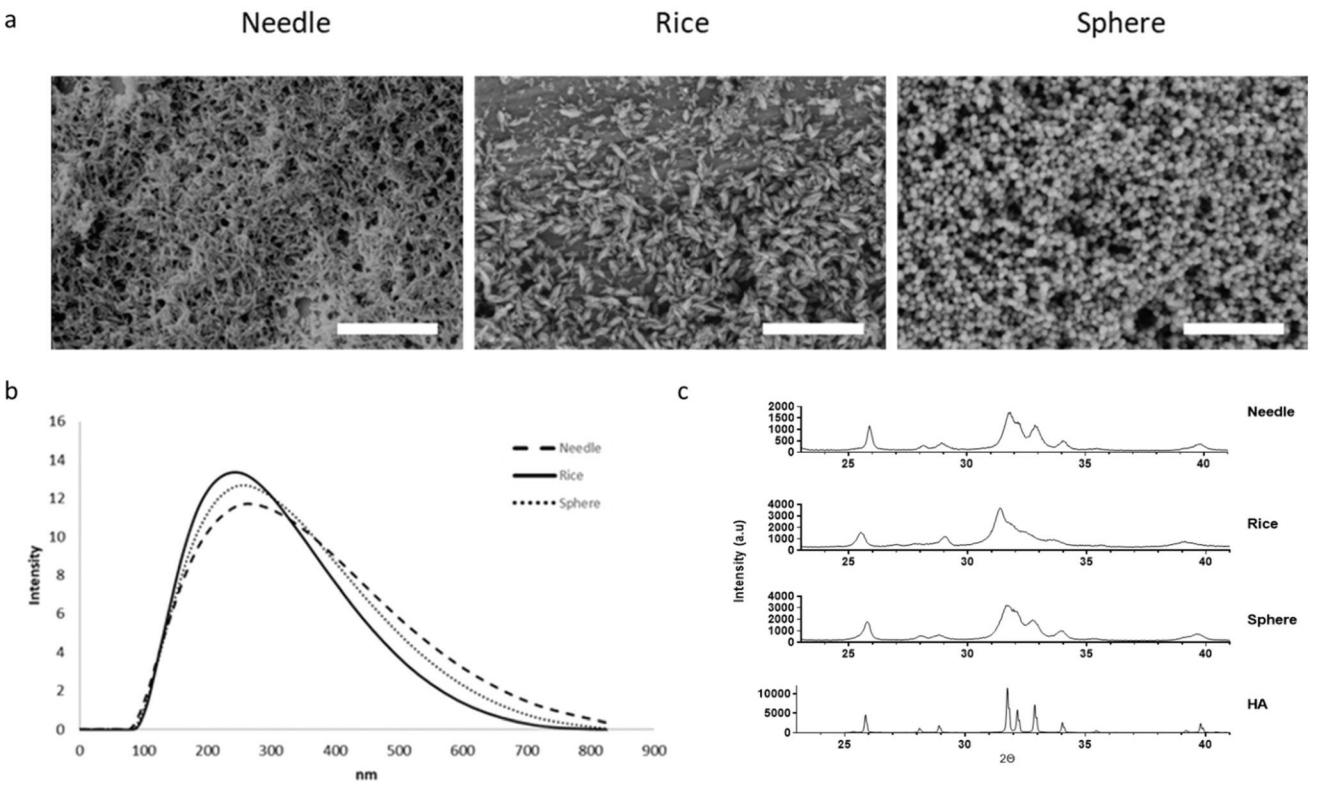

Fig. 1 Needle-, rice- and spherical-shaped nHA were characterized for their morphology, size and crystallinity. (a) SEM images show distinct needle-, rice- and spherical-shaped nHA particles. Scale bar for SEM images is 1 μm. (b) Size of the nHA in ethanol measured by DLS. (c) Crystallinity of nHA: X-ray diffraction patterns of needle, rice and spherical shaped nHA in comparison to commercially bought sintered HA powder. nHA showed diffraction patterns typical of poorly crystalline HA.

mation of nanoparticles that were homogenous in both size and shape. X-ray diffraction analysis showed that the three types of nanoparticles showed patterns typical of HA (Fig. 1c). All particles, and in particular needle shaped nHA showed a low crystallinity.

The HA nanoparticle shape strongly depends on the synthesis method and the parameters of the synthesis process. In general, HA crystals found in natural tissues such as bone and teeth, and HA microparticles precipitated using conventional methods[44,45] have the shape of needles, rods, fibers, or thin plates because of the preferred orientation for growth along the *c*-axis of HA crystals.[46] Needle-shaped HA particles are the most commonly reported and can be achieved *via* different approaches such as hydrothermal processing,[47] microwave-assisted deposition[48] and wet chemical precipitation.[49–54] The latter method is the most widely used due to low cost, simple setup and low temperature required for the synthesis. However, by using the wet chemical precipitation, it remains challenging to obtain nanoparticles with homogenous size and shape, because calcium and phosphate ions can spontaneously precipitate and crystallize above pH 7. To overcome this problem, in the current study, a combination of slow addition of calcium and phosphate ion precursors and phosphate-PEG, an inhibitor of crystal growth, were used to create needle-shaped nHA with homogenous size and shape.

Wet chemical precipitation also allows the addition of surfactants to the reaction mixture that act as directing agents to develop nanoparticles with different shapes, including rice-shaped and spherical HA particles. Here we used CTAB as a surfactant to yield rice-shaped nanoparticles.[55] Finally, to synthesize spherical-shaped nanoparticles, we used MSNs as a template. MSNs are commonly used as delivery vehicles because of their mesoporous structure and, in addition, can be easily surface modified for *e.g.* controlled drug delivery.[56] In particular, deposition of a CaP layer on the MSN surface has been reported for pH-responsive gating of the pores for controlled drug delivery.[57,58] In our study, MSNs were first surface modified to contain carboxylic acid groups (MSN-COOH) and subsequently calcium and phosphate ions were alternately deposited on the MSN-COOH leading to homogeneous-size spherically shaped nanoparticles. Importantly, the MSN-COOH provided a preferred surface for ion deposition, preventing unspecific precipitation of CaP in solution.

3.2. nHA film synthesis and characterization

To construct the films, nHA were deposited onto surface-activated glass cover slips by spin-coating of nanoparticle suspensions in ethanol, as reported previously.[43] SEM imaging revealed the deposition of continuous layers of nanoparticles with a homogeneous surface structure, independent of the nanoparticle shape used (Fig. 2a). The overall roughness and arithmetic average roughness (R_a) were measured using a profilomete. Needle nHA films had the highest R_a value (79 ± 4), followed by rice nHA films (69 ± 3), and spherical nHA films (38 ± 2). An example of this R_a calculation process is shown in ESI (Fig. S1†).

Next, nHA film stability by immersion in PBS (pH 7.4) and cell culture medium was followed over a period of 6 days, and calcium and phosphorus concentrations were measured using ICP-MS (Fig. 2b and c). In PBS, phosphate depletion from the PBS was observed for all nHA films, with no significant difference observed as a function of nHA shape. Furthermore, the same phosphate depletion from the PBS was observed for the plasma treated control glass slides. In contrast, some calcium release from the films was observed in PBS for all three nHA films. This release was immediate, and remained stable over the 6-day period (Fig. 2c). Needle-shaped nHA films showed higher calcium release, followed by rice- and spherical-shaped nHA films. However, the overall amount of calcium release was limited compared to total amount present on the films (less than 1% for each film). In contrast, when the nHA films were immersed in cell culture medium, calcium and phosphate depletion from the cell culture media was observed for all three nHA films as well as for the plasma treated glass slide (Fig. 2d). The calcium depletion from the medium was nHA shape dependent after 24 hours, with needle nHA films showing least calcium depletion, followed by spherical- and rice-shaped nHA films. However, at later time-points calcium depletion was similar for all nHA films as well as for plasma treated glass slides. We also investigated the long-term stability of the needle, sphere, and rice nanoparticle based films over 21 days in media that was exchanged every 3 days to simulate our cell culture conditions. A continuous reduction of calcium and phosphorous from the cell culture media could be observed indicating calcium and phosphate deposition on the films (Fig. S2†). Indeed, calcium and phosphate deposition on the films in the form of brushite crystals could be observed on the nanoparticle films as well as on the glass control slides after 6 days of incubation using SEM imaging (Fig. 2d). Calcium and phosphate ion deposition on the glass slides may be due to its negative charge inferred by the plasma treatment, triggering calcium and phosphate deposition.

The dissolution of HA coatings in non-cellular environments depends on the coating characteristics (including roughness, crystallinity, porosity) and on the buffer conditions (*e.g.* pH, ion concentrations).[59,60] In addition, next to the dissolution of HA there is another competing process; re-precipitation of HA. The precipitation mechanism is mainly dominated by the concentration of calcium and phosphate ions as well as the overall ionic strength of the solution.[59,61,62] The observed differences for calcium between the two conditions may thus be explained by the presence (cell culture medium) and absence (PBS) of calcium in the buffers.

Next, the spherical nanoparticles were labelled with a fluorescent dye in their core (without affecting the surface chemistry of the nanoparticles) and nanoparticle release in media was followed over 7, 14 and 21 days to further investigate nanoparticle film stability. No significant nanoparticle release

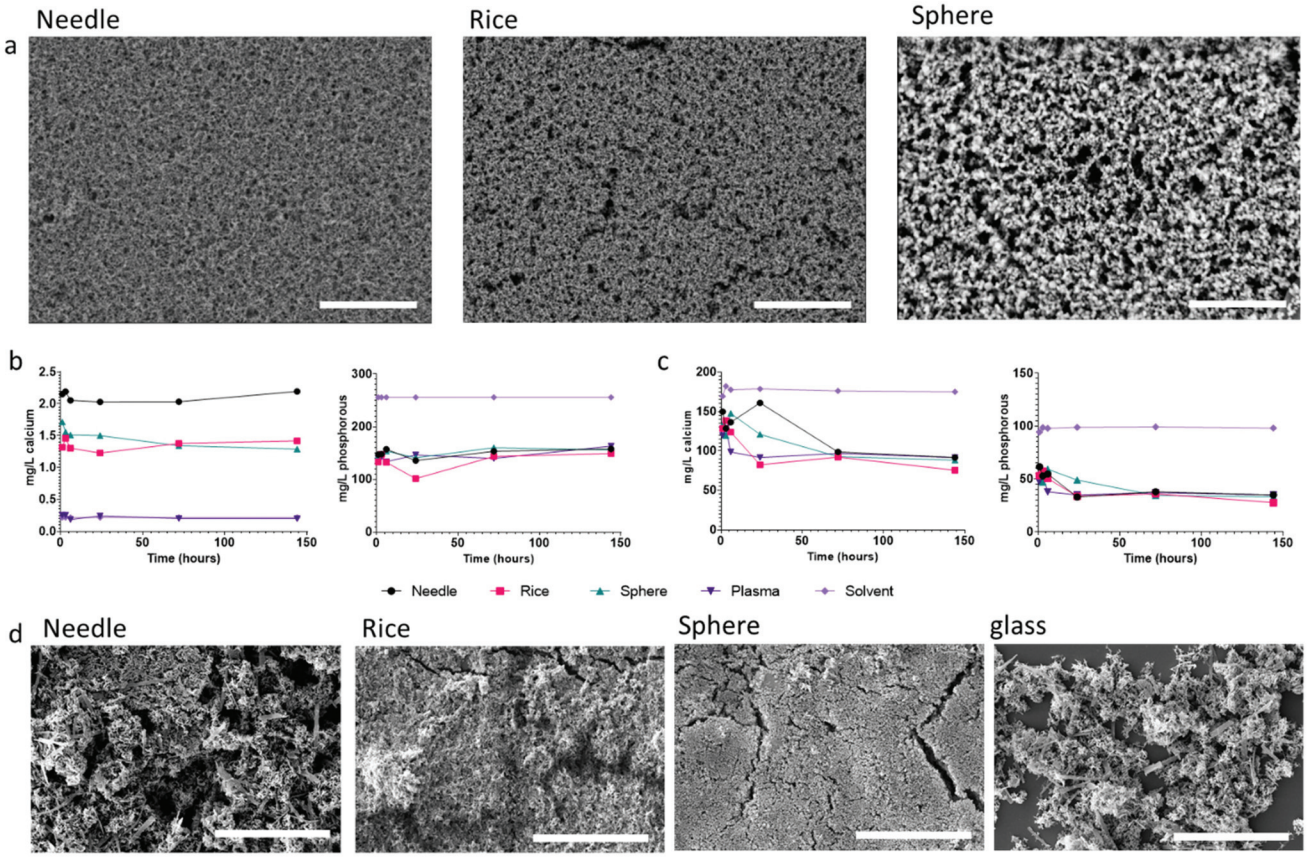

Fig. 2 Characterization of nHA films. (a) Scanning electron microscopy (SEM) images of films deposited using needle-, rice- and spherical-nHA. Scale bars are 5 μm. Calcium and phosphorus concentration profiles after immersion of the nHA films in (b) PBS and (c) cell culture medium. (d) SEM images of needle-, rice-, spherical-nHA film and plasma treated control glass slides after incubated in cell culture media for 6 days. Scale bar is 10 μm.

could be observed (Fig. S3†), further proving the stability of the films.

3.3. Effect of nHA shape on hMSC osteogenic gene and protein expression

To study the effect of nHA shape on the osteogenic differentiation, hMSCs were cultured on films deposited using nHA of different shape and the expression of osteogenic markers RUNX2, BMP2, ALP, OPN, OCN was quantified using qPCR analysis after 7, 14 and 21 days of culture in basic cell culture medium, thus without stimulators of osteogenic differentiation (Fig. 3). Cells cultured on glass slides without nanoparticle coating served as a control.

hMSCs cultured on films of needle- and rice-shaped nHA could significantly induce RUNX2, an early-stage marker of osteoblast differentiation,[63] after 14 days of culture. After 21 days, a significantly upregulated expression of RUNX2 was observed for hMSCs cultured on rice- and spherical-shaped nHA films compared to the control (Fig. 3a).

Rice-shaped nHA-based films also induced early expression (day 7) of BMP2, which plays an important role in MSC differentiation.[64] BMP2 expression remained high even after 21 days of culture. In contrast, needle nHA films only induced significant BMP2 expression after 14 days, which decreased after 21 days, whereas spherical nHA films did not induce any significant BMP2 expression at any of the time-points (Fig. 3b).

ALP is an enzyme which acts as a mineralization promoter, and is usually expressed after 14 and 21 days of culture.[65] On all three films, ALP expression was upregulated only after 21 days of culture, with the highest expression observed on needle nHA films, followed by rice- and spherical nHA films, respectively (Fig. 3c).

Needle- and rice nHA films also induced late osteogenic marker OPN[41] in hMSCs after 14 days, whereas hMSCs cultured on spherical nHA films only showed a significant upregulation of this marker after 21 days of culture. Interestingly, where needle- and rice nHA films induced similar OPN expression after 14 days, after 21 days, needle nHA films showed a significantly higher OPN expression (Fig. 3d).

The expression of osteocalcin (OCN), a calcium binding protein involved in bone mineralization,[66,67] of hMSCs cultured on needle- and rice nHA films was significantly expressed after 14 and 21 days, whereas spherical nHA films

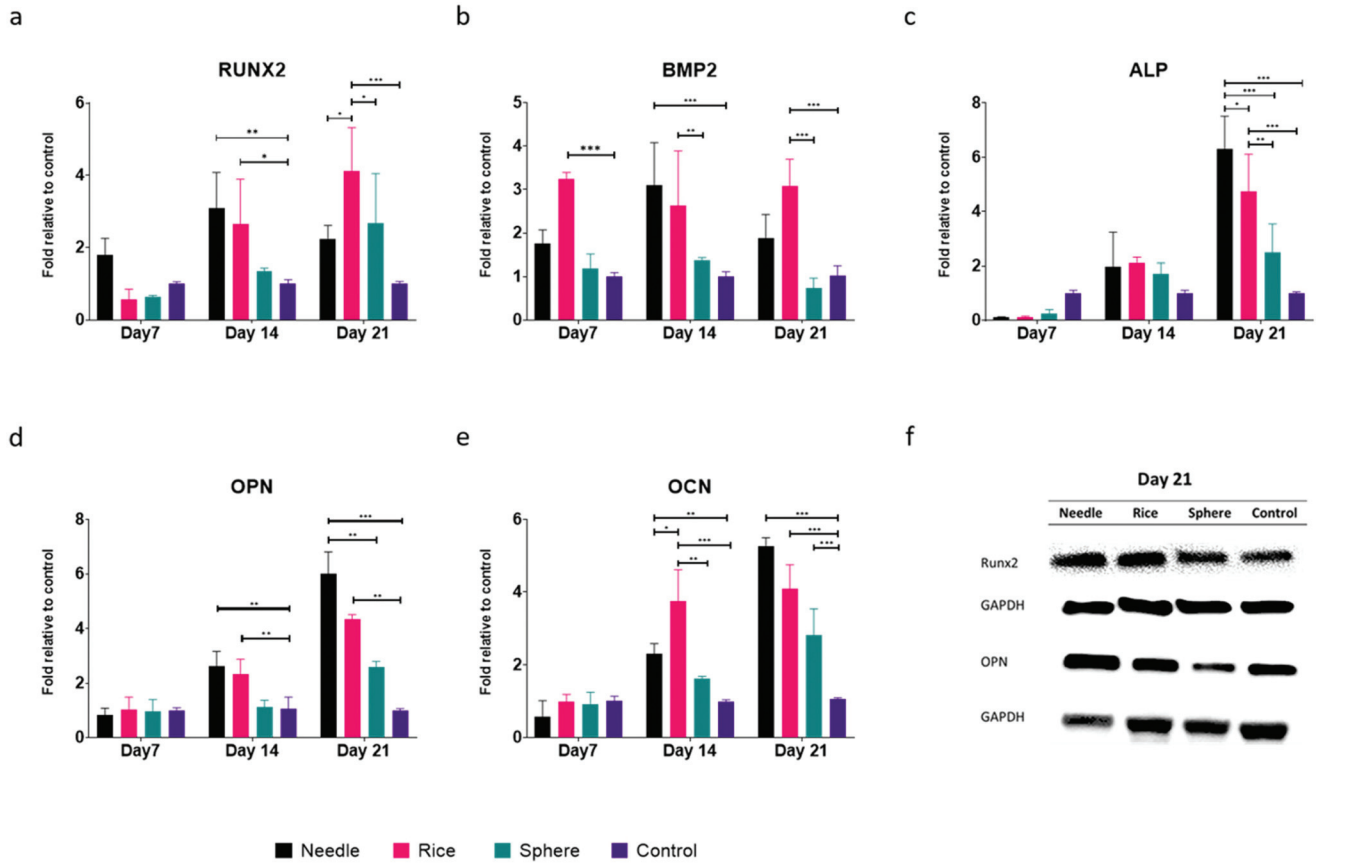

Fig. 3 hMSC osteogenic gene and protein expression as a function of nHA shape. hMSC expression of (a) RUNX2, (b) BMP2, (c) ALP, (d) OPN, (e) OCN cultured on needle- (black), rice- (pink), spherical-shaped (green) nHA films. The results were normalized to GAPDH as housekeeping gene and calibrated to gene expression of hMSCs cultured on plasma treated glass slides (controls, purple). All samples were cultured in basic medium for 7, 14 and 21 days. The significant differences were indicated as follows: $*p < 0.01$; $**p < 0.01$; $***p < 0.001$. (f) Western blot analysis of RUNX2 and OPN protein expression after 21 days of hMSC culture on needle-, rice-, spherical-shaped nHA films or control glass slides.

only significantly induced OCN after 21 days of culture (Fig. 3e).

To confirm that the observed effect on the gene level was also translated to protein level, the effect of nanoparticle shape on hMSCs osteogenic protein expression was investigated for RUNX2 and OPN using Western blot analysis (Fig. 3f). RUNX2 protein expression followed a similar trend as was observed for gene expression. This was also the case for OPN protein expression, with needle-shaped and rice-shaped nanoparticle films showing similar OPN levels after 14 days (Fig. S4†), whereas after 21 days, the OPN expression levels followed the trend needle > rice > sphere (Fig. 3f).

Taken together, overall, all three nHA coated films could induce the expression of osteogenic markers in basic culture conditions. Even though all nHA films showed the ability to induce osteogenic differentiation in hMSCs, we observed that the expression profile and the expression extent was dependent on the shape of the HA nanoparticles used to deposit the films. Regarding differences amongst the three shapes, overall, needle nHA films were most effective in inducing osteogenic gene expression and spherical nHA films least effective. However, for RUNX2, BMP2 and OCN at certain time-points rice nHA films showed higher gene induction compared to spherical and needle nHA films. In addition, needle nHA films showed a different expression pattern for the early markers (RUNX2, BMP2) which were significantly induced after 14 days of hMSC culture and reduced after 21 days of culture. In contrast, no significant induction of BMP2 was observed in hMSCs cultured on spherical nHA films, and hMSCs cultured on rice nHA films resulted in the prolonged expression of RUNX2 and BMP2 even after 21 days of hMSC culture. It has been shown that RUNX2 protein levels are maximal in preosteoblasts and early mature osteoblasts, following a gradual increase during the process of commitment. RUNX2 levels are then decreased significantly in mature osteoblasts and osteocytes, which is in line with our observations of hMSC osteogenic marker expression on needle shaped nHA films. In addition, all three nHA films induced high expression of middle to late osteogenic markers (ALP, OPN and OCN) after 14 and 21 days of hMSC culture which followed the order needle > rice > sphere nHA films.

Next to the nanoparticle shape, the presence of brushite precipitation shown in Fig. 2d could also contribute to the increased osteogenic marker expression observed in the hMSCs. However, these observations were made in an acellular environment and, in addition, brushite precipitation was also observed in the controls (plasma treated glass, Fig. 2d far right). Since osteogenic marker expression were measured relative to the plasma treated glass controls, any additional marker expression can be attributed to the differently shaped nanoparticle films.

Previous studies have shown that stem cells can sense nanotopographies leading to increased osteogenic marker levels.[68–71] Furthermore, it has been shown that nHA, when added directly to the cell culture medium, can induce osteogenesis in hMSCs.[38–40,67] However, there are only a limited amount of studies investigating the effect of HA nanoparticle shape on their ability to induce hMSC osteogenesis.[38–40] One of these studies reported increased upregulation of OCN and ALP markers in hMSCs when exposed to nHA needles compared to spherical nHA.[38] In a similar study it was shown that 50 nm sized HA spheres and nanorods were both osteogenic, however higher upregulation of late osteogenic markers OCN and OPN was observed in hMSCs when exposed to spherical nHA.[39] Although these results highlight that nHA shape is an important factor in their osteogenic capabilities, these studies were performed by adding nHA directly to the medium and not as coated films as studied here.

In summary, all three nanoparticle films studied here induced increased levels of a selection of early, middle and late osteogenic markers at basic culture conditions. However, their expression levels and profiles over time differed significantly as a function of nanoparticle shape, with needle-shaped nanoparticles-based films generally showing highest expression of all tested osteogenic markers.

3.4. nHA coated films *versus* nHA added directly to the cell culture medium

To further investigate the osteogenic effect of the nHA, a new set of experiments was run. Suspension and conditioned medium were compared to the osteogenic capabilities of the nHA films (film) in basic conditions. The needle- and spherical-shaped nanoparticles were added directly to the cell culture medium (32 μg ml^{-1} for needle nanoparticles and 43 μg ml^{-1} for spherical nanoparticle) to create the suspension medium. Conditioned media was created by incubating cell culture media with the nanoparticles overnight, and removing the nanoparticle using centrifugation before addition of the media to the hMSCs. Cells cultured on glass slides again served as a control and basic cell culture medium was used for all groups. Intermediate- and late osteogenic markers expression (ALP, OPN and OCN) were quantified using qPCR analysis after 21 days of culture (Fig. 4).

In accordance to the first set of experiments, hMSCs cultured on both needle- and spherical-shaped nanoparticle films induced significantly higher expression of ALP, OPN and OCN compared to the control. Interestingly, when needle and spherical nHA were added to the cell culture medium as a suspension, no upregulation of ALP and OCN expression was observed. The OPN expression was upregulated, although to a lower extent compared to hMSCs seeded on the nHA films. Cell culture medium conditioned with nHA did not show significant ALP, OPN and OCN expression compared to the control. Thus, nHA films had a higher capacity to induce osteogenic differentiation in hMSCs compared to nHA added as suspension or the nHA conditioned medium.

To our knowledge, a direct comparison of the osteogenic marker expression in hMSCs between surface-immobilized and 'free' nHA has not been done previously. Several studies have reported the osteogenic effect of supplementation of cell culture medium with CaP nanoparticles or with calcium and/or phosphate ions.[41,72–78] While adding nHA as a suspension resulted in a significant increase of OPN compared to the control, this was much lower compared to nHA coated films. Interestingly, also in suspension conditions, needle nHA resulted in higher OPN expression in hMSCs compared to spherical nanoparticles. It should be noted that the concentration of the nanoparticles in suspension used here was

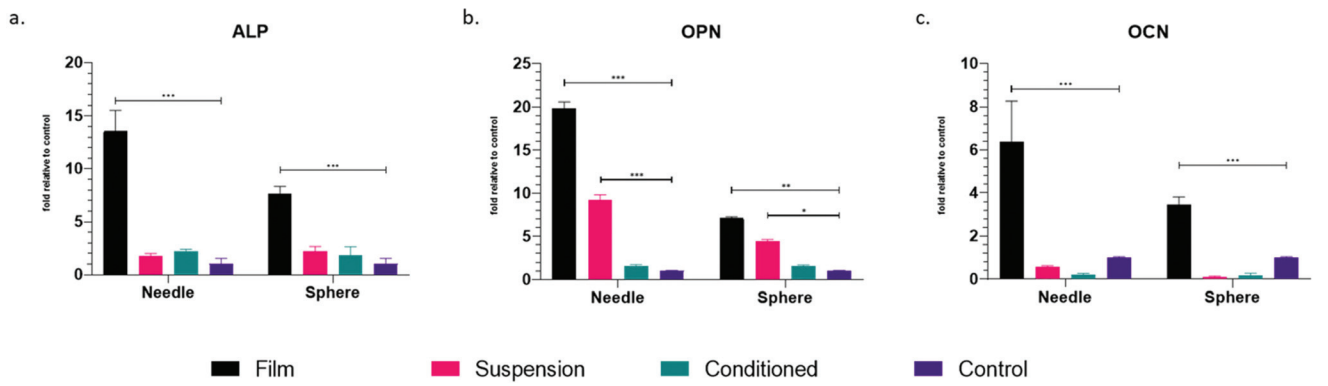

Fig. 4 nHA administration comparison. hMSC expression of (a) ALP, (b) OPN and (c) OCN after 21 days of culture in basic cell culture medium on nHA films (black), exposed to medium containing nanoparticles (pink), exposed to medium conditioned with nanoparticles (green). The results were normalized to GAPDH (housekeeping gene) and calibrated to gene expression levels of hMSCs cultured on plasma treated glass slides (control; blue). The statistically significant differences are indicated as follows: *$p < 0.01$; **$p < 0.01$; ***$p < 0.001$.

32–43 μg ml^{-1} in basic media, whereas in an earlier study, the amount ranged from 10 μg ml^{-1} to 3 mg ml^{-1} in osteogenic media.[79] The chosen concentration in this study was calculated such that the total amount of nHA the hMSCs were exposed to, remained constant across the film and suspension groups. Conditioned media did not lead to any significant upregulation of osteogenic markers, likely because studies that looked into the effect of calcium and phosphate ions on cell behaviour used relatively high ion concentrations in the range of 1.8–50 mM to induce osteogenesis.[73–76]

The osteogenic effects of nHA added to cell culture medium involves their internalization by hMSC, where cell internalization rate and concentration is highly dependent on shape and size of the nHA.[39,79] In our study, the films were stable under cell culture conditions, and no ions were released from the coatings under cell culture conditions (Fig. 2d), indicating that osteogenic induction of hMSCs *via* nHA coatings occurs *via* different pathways compared to adding nHA directly to the medium. In addition, although we kept the total amount of nHA the same across both conditions, in the case of the nanoparticle based films, the MSCs experience the contribution of the nHA already from day one. These considerations makes it difficult to do direct comparisons between the two administration routes. Our results do suggest that adding nHA at relatively low concentrations does not effectively induce osteogenic differentiation of hMSCs in basic conditions, where immobilizing an equal amount of nanoparticles on a surface in the form of a film resulted in significant osteogenic gene expression of hMSCs for both needle- and spherical-shaped nHA (Fig. 4).

3.5. Cell morphology on nanoparticle-based films

To investigate the effect of the nHA shape on cell attachment and morphology, hMSCs were cultured for 3 days on needle, rice and spherical nHA films. Following immunofluorescence staining of cell nuclei, cytoskeleton and focal adhesions, their morphology was characterized in terms of cell area, perimeter, and compactness of cell (irregularity of shape) (see Fig. S5† for image analysis workflow). HMSCs grown on needle nHA films exhibited a significantly larger cell area than the cells cultured on the other two films. The cell area of hMSCs cultured on needle nHA films was 175% and 59% larger compared to hMSCs cultured on rice and spherical nHA films, respectively (Fig. 5a). Also the cell perimeter of hMSCs on needle nHA films was 120% and 76% larger in comparison to hMSCs grown on rice and spherical nHA films, respectively (Fig. 5b). hMSCs cultured on spherical nHA films were overall more irre-

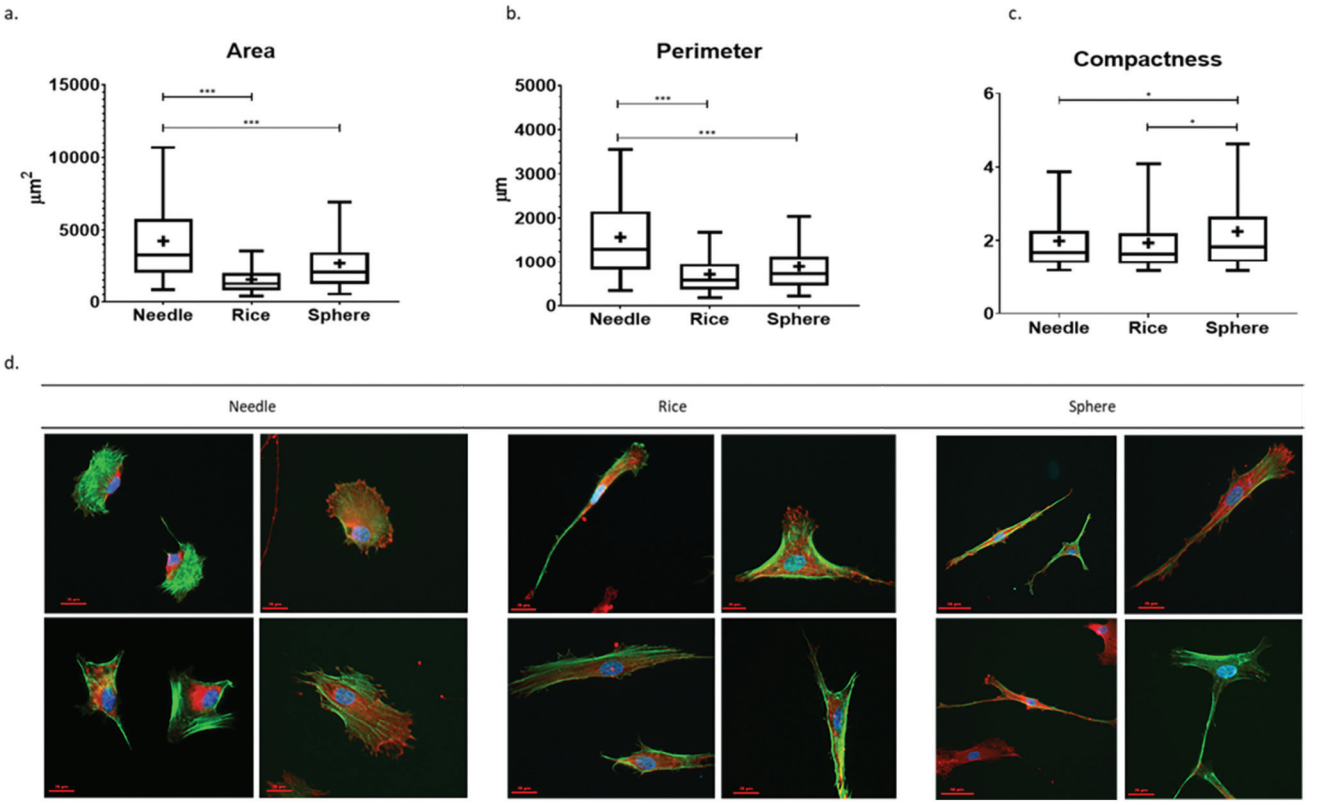

Fig. 5 hMSC morphology on nHA films. Box plots showing the (a) area, (b) perimeter and (c) compactness of hMSCs grown on needle-, rice- and spherical-shaped nHA films for 3 days. The statistically significant differences are indicated as follows: *$p < 0.01$; **$p < 0.01$; ***$p < 0.001$. Upper border and lower border of the boxes are third quartile and first quartile respectively. + indicates the mean of each data group. (d) Fluorescence microscopy images of focal adhesions of hMSCs cultured on nHA films after 3 days of culture; green represents actin (phalloidin), red represents focal adhesions (vinculin) and blue represents nuclei (DAPI) staining.

gularly shaped as indicated by a compactness that was 11% and 13.7% higher compared to needle and rice nHA films, respectively (Fig. 5c).

Stem cell attachment mainly occurs through bundling of focal adhesion proteins such as vinculin.[80,81] Therefore, the formation of focal adhesions of hMSCs on the nanoparticle films was observed using fluorescence microscopy imaging of vinculin staining. A typical hMSC morphology with extended filopodia could be observed for hMSCs grown on needle nHA films (Fig. 5d) that was very similar to hMSCs grown on glass slides exposed to osteogenic media (Fig. S6b†). In comparison, hMSCs grown on rice and spherical nHA films showed less extended filopodia. Especially in the case of spherical-shaped nanoparticle films, hMSCs showed elongation in one or two directions (Fig. 5d) which showed similar morphology to hMSCs grown on glass slides in basic conditions (Fig. S6a†).

In summary, we observed a larger cell area and perimeter of hMSCs cultured on needle-shaped nHA films, indicating a more pronounced spreading compared to hMSCs cultured on rice and spherical nHA films. hMSC spreading has been correlated to enhanced osteogenic differentiation of hMSCs,[82–85] mediated by intracellular tension and mechanical changes in the cytoskeleton sending signals *via* contractile forces to the nucleus.[86,87] Here, hMSCs cultured on needle-shaped nanoparticle films showed increased cell spreading which correlated with the upregulation of markers of osteogenic differentiation. However, even though hMSCs cultured on rice nHA showed less cell spreading, rice nHA films were effective in inducing osteogenic differentiation.

Higher compactness and elongation was observed for hMSCs seeded on spherical nHA films in comparison to needle and rice nHA films. Higher hMSC compactness suggests a less pronounced formation of filopodia in hMSCs seeded on spherical nHA films. Similar to our findings, Zhao *et al.*[88] showed that osteoblast cultured on spherical nHA exhibited an elongated morphology, while osteoblasts cultured on rod shaped nHA showed an increased number of filopodia.

4. Conclusions

Here we showed that hMSCs cultured on needle, rice and spherical nHA films could efficiently induce the expression of osteogenic markers in the absence of other osteogenic stimulators. Although all three nHA films had a stimulatory effect, differences in their potential to promote osteogenesis *in vitro* was observed. In particular, needle nHA films induced the expression of early osteogenic markers RUNX2 and BMP2 after 14 days, whereas rice nHA induced late induction of BMP2 and RUNX2 in hMSCs. In addition, needle nHA films showed a higher induction of late markers (ALP, OCN and OPN) compared to spherical and rice-shaped nanoparticle films. Spherical nHA films were least efficient in inducing osteogenesis in hMSCs *in vitro*.

Previously it has been shown that nHA can induce osteogenesis in hMSCs when added directly to cell culture media in high concentrations. Here we showed that nHA in the form of stable films can efficiently promote osteogenic marker expression in hMSCs. The pronounced positive effect of nHA films on osteogenic differentiation of hMSCs, with in particular the needle nHA films, is plausibly related to the initial adhesion and spreading of the hMSCs on these films. We observed that hMSCs seeded on needle nHA films showed a typical hMSC morphology with extended filopodia.

The results of this study suggest that the coatings based on homogeneously synthesized needle-shaped nHA may be a promising strategy for improving bioactivity of biomedical implants, like the biocompatible but bioinert metallic implants used in orthopedics and maxillofacial surgery. Indeed, nHA have been used as coatings to promote bone ingrowth and enhance osteointegration.[89,90] Additional understanding of how (nano)particle shape influences the bioactivity of these coatings will enhance their efficiency and potentially expand their applicability.

Conflicts of interest

The authors have declared that no competing interest exists.

Acknowledgements

We thank Denis van Beurden for technical assistance with SEM imaging and Dr Eva Gubbins for technical assistance with ICP-MS. This research was financially supported by the Gravitation Program “Materials Driven Regeneration”, funded by the Netherlands Organization for Scientific Research (024.003.013) and Royal Thai Government Scholarship Program (offered by OCSC).

References

1 M. Nagano, T. Nakamura, T. Kokubo, M. Tanahashi and M. Ogawa, *Biomaterials*, 1996, **17**, 1771–1777.
2 D. Apelt, F. Theiss, A. El-Warrak, K. Zlinszky, R. Bettschart-Wolfisberger, M. Bohner, S. Matter, J. A. Auer and B. von Rechenberg, *Biomaterials*, 2004, **25**, 1439–1451.
3 S. K. Ghosh, S. K. Nandi, B. Kundu, S. Datta, D. K. De, S. K. Roy and D. Basu, *J. Biomed. Mater. Res., Part B*, 2008, **86**, 217–227.
4 R. Z. LeGeros, *Chem. Rev.*, 2008, **108**, 4742–4753.
5 F. Barrère, C. A. van Blitterswijk and K. de Groot, *Int. J. Nanomed.*, 2006, **1**, 317.
6 S. Utara and J. Klinkaewnarong, *Ceram. Int.*, 2015, **41**, 14860–14867.
7 Y. Su, S. Komasa, P. Li, M. Nishizaki, L. Chen, C. Terada, S. Yoshimine, H. Nishizaki and J. Okazaki, *Int. J. Nanomed.*, 2017, **12**, 925.
8 D.-X. Wang, Y. He, L. Bi, Z.-H. Qu, J.-W. Zou, Z. Pan, J.-J. Fan, L. Chen, X. Dong and X.-N. Liu, *Int. J. Nanomed.*, 2013, **8**, 1855.

9 W. Wang, S. Itoh, Y. Tanaka, A. Nagai and K. Yamashita, *Acta Biomater.*, 2009, **5**, 3132–3140.
10 P. Habibovic, T. M. Sees, M. A. van den Doel, C. A. van Blitterswijk and K. de Groot, *J. Biomed. Mater. Res., Part A*, 2006, **77**, 747–762.
11 A. Hofmann, L. Konrad, L. Gotzen, H. Printz, A. Ramaswamy and C. Hofmann, *J. Biomed. Mater. Res., Part A*, 2003, **67**, 191–199.
12 K. Ogata, S. Imazato, A. Ehara, S. Ebisu, Y. Kinomoto, T. Nakano and Y. Umakoshi, *J. Biomed. Mater. Res., Part A*, 2005, **72**, 127–135.
13 D. Richard, N. Dumelié, H. Benhayoune, S. Bouthors, C. Guillaume, N. Lalun, G. Balossier and D. Laurent-Maquin, *J. Biomed. Mater. Res., Part B*, 2006, **79**, 108–115.
14 L. W. Lin, K. L. Chow and Y. Leng, *Key Eng. Mater.*, 2008, 1005–1008.
15 R. Shu, R. McMullen, M. Baumann and L. McCabe, *J. Biomed. Mater. Res., Part A*, 2003, **67**, 1196–1204.
16 F. Barrere, C. Van Der Valk, G. Meijer, R. Dalmeijer, K. De Groot and P. Layrolle, *J. Biomed. Mater. Res., Part B*, 2003, **67**, 655–665.
17 R. Jimbo, P. G. Coelho, S. Vandeweghe, H. O. Schwartz-Filho, M. Hayashi, D. Ono, M. Andersson and A. Wennerberg, *Acta Biomater.*, 2011, **7**, 4229–4234.
18 J. W. Durham III, S. A. Montelongo, J. L. Ong, T. Guda, M. J. Allen and A. Rabiei, *Mater. Sci. Eng., C*, 2016, **68**, 723–731.
19 C. Chen, H. Li, C. Guo and S. Chen, *Exp. Ther. Med.*, 2016, **12**, 302–306.
20 Z. Othman, B. Cillero Pastor, S. van Rijt and P. Habibovic, *Biomaterials*, 2018, **167**, 191–204.
21 Z. Othman, R. J. Mohren, B. Cillero-Pastor, Z. Shen, Y. S. Lacroix, A. P. Guttenplan, Z. T. Birgani, L. Eijssen, T. M. Luider and S. van Rijt, *Mater. Today Bio*, 2020, 100066.
22 R. Jimbo, P. G. Coelho, M. Bryington, M. Baldassarri, N. Tovar, F. Currie, M. Hayashi, M. N. Janal, M. Andersson and D. Ono, *J. Dent. Res.*, 2012, **91**, 1172–1177.
23 S. R. Paital and N. B. Dahotre, *Mater. Sci. Eng., R*, 2009, **66**, 1–70.
24 C. Danoux, L. Sun, G. Koçer, Z. T. Birgani, D. Barata, J. Barralet, C. van Blitterswijk, R. Truckenmüller and P. Habibovic, *Adv. Mater.*, 2016, **28**, 1803–1808.
25 G. Thakral, R. Thakral, N. Sharma, J. Seth and P. Vashisht, *J. Clin. Diagn. Res.*, 2014, **8**, ZE07.
26 T. J. Webster, C. Ergun, R. H. Doremus, R. W. Siegel and R. Bizios, *Biomaterials*, 2000, **21**, 1803–1810.
27 L. G. Gutwein and T. J. Webster, *Biomaterials*, 2004, **25**, 4175–4183.
28 H. V. Unadkat, M. Hulsman, K. Cornelissen, B. J. Papenburg, R. K. Truckenmüller, A. E. Carpenter, M. Wessling, G. F. Post, M. Uetz and M. J. Reinders, *Proc. Natl. Acad. Sci. U. S. A.*, 2011, **108**, 16565–16570.
29 H. S. Alghamdi, R. Bosco, S. K. Both, M. Iafisco, S. C. Leeuwenburgh, J. A. Jansen and J. J. van den Beucken, *Biomaterials*, 2014, **35**, 5482–5490.
30 D. Alves Cardoso, J. Jansen and S. G. Leeuwenburgh, *J. Biomed. Mater. Res., Part B*, 2012, **100**, 2316–2326.
31 H. Urch, C. Geismann, M. Ulbricht and M. Epple, *Materialwiss. Werkstofftech.*, 2006, **37**, 422–425.
32 M. Epple, K. Ganesan, R. Heumann, J. Klesing, A. Kovtun, S. Neumann and V. Sokolova, *J. Mater. Chem.*, 2010, **20**, 18–23.
33 T. J. Levingstone, S. Herbaj and N. J. Dunne, *Nanomaterials*, 2019, **9**, 1570.
34 N. Kantharia, S. Naik, S. Apte, M. Kheur, S. Kheur and B. Kale, *Bone*, 2014, **34**, 171.
35 S. Koutsopoulos, *J. Biomed. Mater. Res.*, 2002, **62**, 600–612.
36 Q. Lv, L. Nair and C. T. Laurencin, *J. Biomed. Mater. Res., Part A*, 2009, **91**, 679–691.
37 G. E. Poinern, R. K. Brundavanam, N. Mondinos and Z.-T. Jiang, *Ultrason. Sonochem.*, 2009, **16**, 469–474.
38 J. Xu, K. A. Khor, J. Sui, J. Zhang and W. N. Chen, *Biomaterials*, 2009, **30**, 5385–5391.
39 J. Wang, G. Yang, Y. Wang, Y. Du, H. Liu, Y. Zhu, C. Mao and S. Zhang, *Biomacromolecules*, 2015, **16**, 1987–1996.
40 Y. Liu, G. Wang, Y. Cai, H. Ji, G. Zhou, X. Zhao, R. Tang and M. Zhang, *J. Biomed. Mater. Res., Part A*, 2009, **90**, 1083–1091.
41 E. D. Jensen, R. Gopalakrishnan and J. J. Westendorf, *BioFactors*, 2010, **36**, 25–32.
42 R. Rosenbrand, D. Barata, P. Sutthavas, R. Mohren, B. Cillero-Pastor, P. Habibovic and S. van Rijt, *Int. J. Nanomed.*, 2018, **13**, 7711.
43 L. Andrée, D. Barata, P. Sutthavas, P. Habibovic and S. van Rijt, *Acta Biomater.*, 2019, **96**, 557–567.
44 H. Zhou and J. Lee, *Acta Biomater.*, 2011, **7**, 2769–2781.
45 A. Haider, S. Haider, S. S. Han and I.-K. Kang, *RSC Adv.*, 2017, **7**, 7442–7458.
46 M. Aizawa, T. Matsuura and Z. Zhuang, *Biol. Pharm. Bull.*, 2013, **36**, 1654–1661.
47 R. Zhu, R. Yu, J. Yao, D. Wang and J. Ke, *J. Alloys Compd.*, 2008, **457**, 555–559.
48 A. Siddharthan, S. Seshadri and T. S. Kumar, *Trends Biomater. Artif. Organs*, 2005, **18**, 110–113.
49 P. Wang, C. Li, H. Gong, X. Jiang, H. Wang and K. Li, *J. Powder Technol.*, 2010, **203**, 315–321.
50 W. Wijesinghe, M. Mantilaka, E. Premalal, H. Herath, S. Mahalingam, M. Edirisinghe, R. Rajapakse and R. Rajapakse, *Mater. Sci. Eng., C*, 2014, **42**, 83–90.
51 A. Paz, D. Guadarrama, M. López, J. E. González, N. Brizuela and J. Aragón, *Quim. Nova*, 2012, **35**, 1724–1727.
52 S. C. Cox, P. Jamshidi, L. M. Grover and K. K. Mallick, *J. Mater. Sci.: Mater. Med.*, 2014, **25**, 37–46.
53 H. Eslami, H. M. Soulati and M. Tahriri, *Iran. J. Pharm. Sci.*, 2008, **4**, 127–134.
54 S. Sagadevan and A. Dakshnamoorthy, *Int. J. Phys. Sci.*, 2013, **8**, 1639–1645.
55 K. Shiba, S. Motozuka, T. Yamaguchi, N. Ogawa, Y. Otsuka, K. Ohnuma, T. Kataoka and M. Tagaya, *Cryst. Growth Des.*, 2016, **16**, 1463–1471.

56 E. Aznar, M. Oroval, L. Pascual, J. R. Murguía, R. Martinez-Manez and F. Sancenon, *Chem. Rev.*, 2016, **116**, 561–718.
57 C. Yang, W. Guo, L. Cui, D. Xiang, K. Cai, H. Lin and F. Qu, *Mater. Sci. Eng., C*, 2014, **36**, 237–243.
58 C.-X. Zhao, L. Yu and A. P. Middelberg, *J. Mater. Chem. B*, 2013, **1**, 4828–4833.
59 A. Afshar, M. Ghorbani and M. Saeri, *J. Ceram. Soc. Jpn.*, 2004, **112**, 77–81.
60 Z. Mohammadi, A. Ziaei-Moayyed and A. S.-M. Mesgar, *Biomed. Mater.*, 2008, **3**, 015006.
61 S. Vahabzadeh, M. Roy, A. Bandyopadhyay and S. Bose, *Acta Biomater.*, 2015, **17**, 47–55.
62 F. Fazan and P. M. Marquis, *J. Mater. Sci.: Mater. Med.*, 2000, **11**, 787–792.
63 T. Komori, in *Osteoimmunology*, Springer, 2009, pp. 43–49.
64 T. Matsubara, K. Kida, A. Yamaguchi, K. Hata, F. Ichida, H. Meguro, H. Aburatani, R. Nishimura and T. Yoneda, *J. Biol. Chem.*, 2008, **283**, 29119–29125.
65 E. E. Golub and K. Boesze-Battaglia, *Curr. Opin. Orthop.*, 2007, **18**, 444–448.
66 J. B. Lian and C. M. Gundberg, *Clin. Orthop. Relat. Res.*, 1988, **226**, 267–291.
67 M. L. Zoch, T. L. Clemens and R. C. Riddle, *Bone*, 2016, **82**, 42–49.
68 F. F. Hulshof, Y. Zhao, A. Vasilevich, N. R. Beijer, M. de Boer, B. J. Papenburg, C. van Blitterswijk, D. Stamatialis and J. de Boer, *Acta Biomater.*, 2017, **62**, 188–198.
69 M. Hulsman, F. Hulshof, H. Unadkat, B. J. Papenburg, D. F. Stamatialis, R. Truckenmüller, C. Van Blitterswijk, J. De Boer and M. J. Reinders, *Acta Biomater.*, 2015, **15**, 29–38.
70 S. Vermeulen and J. de Boer, *Methods*, 2020, DOI: 10.1016/j.ymeth.2020.04.004.
71 S. Kumari, S. Vermeulen, B. Van Der Veer, A. Carlier, J. De Boer and D. Subramanyam, *Tissue Eng., Part B*, 2018, **24**, 255–266.
72 M. Zayzafoon, *J. Cell. Biochem.*, 2006, **97**, 56–70.
73 L. M. Schäck, S. Noack, R. Winkler, G. Wißmann, P. Behrens, M. Wellmann, M. Jagodzinski, C. Krettek and A. Hoffmann, *PLoS One*, 2013, **8**, e65943.
74 C. B. Danoux, D. C. Bassett, Z. Othman, A. I. Rodrigues, R. L. Reis, J. E. Barralet, C. A. van Blitterswijk and P. Habibovic, *Acta Biomater.*, 2015, **17**, 1–15.
75 A. M. Barradas, H. A. Fernandes, N. Groen, Y. C. Chai, J. Schrooten, J. van de Peppel, J. P. van Leeuwen, C. A. van Blitterswijk and J. de Boer, *Biomaterials*, 2012, **33**, 3205–3215.
76 S. Nakamura, T. Matsumoto, J.-I. Sasaki, H. Egusa, K. Y. Lee, T. Nakano, T. Sohmura and A. Nakahira, *Tissue Eng., Part A*, 2010, **16**, 2467–2473.
77 G. R. Beck Jr., *J. Cell. Biochem.*, 2003, **90**, 234–243.
78 Y. C. Chai, S. J. Roberts, J. Schrooten and F. P. Luyten, *Tissue Eng., Part A*, 2011, **17**, 1083–1097.
79 X. Yang, Y. Li, X. Liu, R. Zhang and Q. Feng, *Stem Cells Int.*, 2018, 1–10.
80 A. Carisey and C. Ballestrem, *Eur. J. Cell Biol.*, 2011, **90**, 157–163.
81 K. Collins, E. Gates, C. Gilchrist and B. Hoffman, in *Bio-Instructive Scaffolds for Musculoskeletal Tissue Engineering and Regenerative Medicine*, Elsevier, 2017, pp. 3–35.
82 M. J. Biggs, R. G. Richards, N. Gadegaard, C. D. Wilkinson, R. O. Oreffo and M. J. Dalby, *Biomaterials*, 2009, **30**, 5094–5103.
83 M. D. Treiser, E. H. Yang, S. Gordonov, D. M. Cohen, I. P. Androulakis, J. Kohn, C. S. Chen and P. V. Moghe, *Proc. Natl. Acad. Sci. U. S. A.*, 2010, **107**, 610–615.
84 C. Seiler, A. Gazdhar, M. Reyes, L. M. Benneker, T. Geiser, K. A. Siebenrock and B. Gantenbein-Ritter, *J. Tissue Eng. Regener. Med.*, 2014, **8**, 737–746.
85 F. Matsuoka, I. Takeuchi, H. Agata, H. Kagami, H. Shiono, Y. Kiyota, H. Honda and R. Kato, *PLoS One*, 2013, **8**, e55082.
86 N. Wang, J. D. Tytell and D. E. Ingber, *Nat. Rev. Mol. Cell Biol.*, 2009, **10**, 75–82.
87 A. Elosegui-Artola, I. Andreu, A. E. Beedle, A. Lezamiz, M. Uroz, A. J. Kosmalska, R. Oria, J. Z. Kechagia, P. Rico-Lastres, A. L. Le Roux, C. M. Shanahan, X. Trepat, D. Navajas, S. Garcia-Manyes and P. Roca-Cusachs, *Cell*, 2017, **171**, 1397–1410.e14.
88 Y. Zhao, Y. Zhang, F. Ning, D. Guo and Z. Xu, *J. Biomed. Mater. Res., Part B*, 2007, **83**, 121–126.
89 J. Wang, M. Wang, F. Chen, Y. Wei, X. Chen, Y. Zhou, X. Yang, X. Zhu, C. Tu and X. Zhang, *Int. J. Nanomed.*, 2019, **14**, 7987.
90 S.-I. Roohani-Esfahani, S. Nouri-Khorasani, Z. Lu, R. Appleyard and H. Zreiqat, *Biomaterials*, 2010, **31**, 5498–5509.

